Spectral and polarimetric characterization of the Gas Pixel Detector filled with dimethyl ether

F. Muleri[a,*], P. Soffitta[a], L. Baldini[b], R. Bellazzini[b], A. Brez[b], E. Costa[a],
S. Fabiani[a,c], F. Krummenacher[d], L. Latronico[b], F. Lazzarotto[a], M. Minuti[b],
M. Pinchera[b], A. Rubini[a], C. Sgró[b], G. Spandre[b]

[a]*IASF/INAF, Via del Fosso del Cavaliere 100, I-00133 Roma, Italy*
[b]*INFN sez. Pisa, Largo B. Pontecorvo 3, I-56127 Pisa, Italy*
[c]*Università di Roma "Tor Vergata", Dipartimento di Fisica, via della Ricerca Scientifica 1, I-00133 Roma, Italy*
[d]*EPFL, Route Cantonale CH-1015 Lausanne, Switzerland*

Abstract

The Gas Pixel Detector belongs to the very limited class of gas detectors optimized for the measurement of X-ray polarization in the emission of astrophysical sources. The choice of the mixture in which X-ray photons are absorbed and photoelectrons propagate, deeply affects both the energy range of the instrument and its performance in terms of gain, track dimension and ultimately, polarimetric sensitivity. Here we present the characterization of the Gas Pixel Detector with a 1 cm thick cell filled with dimethyl ether (DME) at 0.79 atm, selected among other mixtures for the very low diffusion coefficient. Almost completely polarized and monochromatic photons were produced at the calibration facility built at INAF/IASF-Rome exploiting Bragg diffraction at nearly 45 degrees. For the first time ever, we measured the modulation factor and the spectral capabilities of the instrument at energies as low as 2.0 keV, but also at 2.6 keV, 3.7 keV, 4.0 keV, 5.2 keV and 7.8 keV. These measurements cover almost completely the energy range of the instrument and allows to compare the sensitivity achieved with that of the standard mixture, composed of helium and DME.

Keywords: X-rays, Gas Detectors, Polarimetry
PACS: 29.40.Cs, 07.85.Fv, 95.55.Ka, 95.75.Hi

1. Introduction

Detectors able to image charged particle tracks in a gas have been developed over the last few years for different applications. One of the most promising is the possibility to resolve the path of photoelectrons emitted in the gas in consequence of a photoelectric absorption. The reconstruction of the initial

---

direction of photoelectron emission opens the way for measuring the state of polarization of the absorbed photons because the former is modulated with respect to the direction of the photon electric field with a $\cos^2$ dependency. This makes the photoelectric effect a good analyzer of X-ray polarization, and a perfect one for absorption from spherically symmetric shells.

Only a few gas detectors can resolve so finely the photoelectron tracks to accurately reconstruct the initial direction of emission (Bellazzini et al., 2006; Black et al., 2007). One of the most sensitive is the Gas Pixel Detector (GPD hereafter), developed by INFN-Pisa and INAF/IASF-Rome (Costa et al., 2001; Bellazzini et al., 2007) and currently inserted in the focal plane of several future satellite missions (Bellazzini et al., 2010 in press; Costa et al., 2010 in press). The gas cell is 1 cm or 2 cm thick and a number of mixtures of helium, neon or argon and dimethyl ether (DME hereafter) at 1 atm or 2 atm have been used, the choice of the gas being of fundamental importance for the polarimetric performance of the detector. A hard limit to the lower energy threshold of the instrument is about twice the binding K-shell energy of the absorbing component because above this threshold the photoelectron track, modulated with polarization, prevails on the isotropic one of the Auger electron. Photoelectron range is determined by density, while the average atomic number fixes the mean free path for scatterings with atomic nuclei, which is the length scale on which polarimetric information is smeared. The diffusion coefficient influences the blurring of the photoelectron track during drift in the gas cell and eventually the possibility to resolve the initial part of the photoelectron path and reconstruct correctly the direction of emission. We developed a Monte Carlo software to easily explore the behavior of the instrument to different mixtures and to subsequently test a subset of the most interesting ones.

Recently Muleri et al. (2008) measured the modulation factor μ, namely the amplitude of the response of the instrument for completely polarized photons, for the GPD filled with helium 20% and DME 80% at 2.6 keV, 3.7 keV and 5.2 keV. This data confirmed that measured values are basically consistent with what is expected on the basis of the Monte Carlo software and proved that X-ray polarimetry in Astrophysics with the GPD is feasible. In this paper we characterize the behavior of the GPD with a different gas, i.e. pure DME at 0.79 atm. In particular, we describe the configuration of the GPD and the calibration sources we used in Section 2, while spectral capabilities of the instrument are discussed in Section 3. The measurement of the modulation factor between 2.0 keV and 7.8 keV is reported in Section 4, together with the comparison with Monte Carlo results and what was reported previously on the He 20% and DME 80% mixture. Note that this is the first time that the modulation factor of a gas polarimeter is presented at energies as low as 2.0 keV.

2. Set-up

2.1. Detector configuration

The Gas Pixel Detector is composed of a sealed 1 cm thick gas cell enclosed by a 50 μm beryllium window, a GEM (Gas Electron Multiplier, Sauli,

1997) which collects and amplifies primary electrons produced by photoelectrons in the gas cell, and a finely subdivided pixelized detector (Costa et al., 2001; Bellazzini et al., 2007). The last component, based on a VLSI ASIC realized in 0.18 μm CMOS technology, is the actual breakthrough of the instrument (Bellazzini et al., 2006), which otherwise is fundamentally an array of standard yet exceptionally small independent proportional counters. The top metal layer of the CMOS is fully pixellated to collect the charge produced in the common gas volume and allows to obtain a true 2D image of the photoelectron track even at low energy, thanks to the small (50 μm) pixel size. The acquisition is self-triggered and only a small window of about a thousand of pixels enclosing the track is actually read-out in place of the whole matrix. The chip is 15×15 mm^2 and comprises 105,600 pixels arranged in a hexagonal pattern.

The cell is sealed but can be refilled to test different gases and typically mixtures of helium, neon or argon and DME are used. DME is used to reduce diffusion and also as a quencher, but it acts as the actual absorber in the case of helium mixtures. The first application of the instrument in Astrophysics is expected in the 2-10 keV energy range and within this interval the standard mixture is helium 20% and DME 80% (Muleri et al., 2008). This was preferred to mixtures of neon because of the longer photoelectron path and lower diffusion for equivalent efficiency, which assure a higher polarimetric sensitivity at low energy where the largest part of photons are concentrated. In this paper we push the use of low-diffusion mixtures to the extreme, exploring the use of a pure DME gas at 0.79 atm (0.8 bar). Since helium is basically transparent to X-rays in the 2-10 keV energy range, we expect a sensitivity comparable to the standard mixture, with a possible enhancement because of the lower diffusion.

An improvement with respect to previous versions of the GPD is the use of a laser-etched GEM made of liquid crystal polymer which shows a better temporal gain stability (Tamagawa et al., 2009). A drawback is that the smallest pitch available was only 80 μm (instead of 50 μm of previous detectors), and this has proved to be insufficient to avoid the emergence of systematic effects due to undersampling of short tracks, discussed and removed, as explained in Section 4.1. GEMs with smaller pitch are now in production and will be used for the next GPD prototype. Moreover the thickness is 100 μm instead of 50 μm.

The characteristics of the GPD used are summarized in Table 1.

2.2. Calibration facility

The GPD was characterized at the X-ray facility built at INAF/IASF-Rome. Although its detailed description is beyond the scope of this paper, in the following we briefly present what is relevant to measurements presented below.

Polarized and monochromatic X-rays are produced by Bragg diffraction at 45° (Evans et al., 1977). Incident radiation on a crystal can be decomposed in two components, polarized parallel (π-component) and perpendicularly (σ-component) to the diffraction plane. The latter is more effectively diffracted because the ratio k between the integrated reflectivity of the π and σ components is always smaller than 1. Hence diffracted radiation is (partially) polarized and

Area:	15×15 mm^2
Active area fill fraction:	92%
Window:	50 μm, beryllium
Mixture:	DME 100%, 0.79 atm (0.8 bar)
Cell thickness:	1 cm
GEM material:	copper-coated liquid crystal polymer
GEM pitch:	80 μm
GEM holes diameters:	48 μm
GEM thickness:	100 μm
GEM voltages:	V$_{drift}$=3200 V, V$_{top}$=1145 V, V$_{bottom}$=500 V
Gain:	500
Pixels:	300×352, hexagonal pattern
Pixel noise:	50 electrons ENC
Full-scale linear range:	30000 electrons
Peaking time:	3-10 μs, externally adjustable
Trigger mode:	internal, external or self-trigger
Self-trigger threshold:	2000 electrons
Pixel trigger mask:	individual

Table 1: Main characteristics of the GPD prototype studied in this paper.

the degree of polarization $\mathcal{P}$ is:

$$\mathcal{P} = \frac{1-k}{1+k}. \tag{1}$$

If the incident angle θ is 45°, $k = 0$ and consequently $\mathcal{P} = 1$. For intermediate values, k can be calculated and the value as a function of θ is reported in Figure 1(a) for graphite crystals. The large dependence of k on the incident angle requires the value of θ to be tightly constrained to prevent the dilution of the average degree of polarization (cf. Figure 1(b)). The angular constraint also selects the energy of diffracted radiation, related to θ by Bragg's Law:

$$E(\theta) = \frac{nhc}{2d \sin \theta}, \tag{2}$$

where h and c are respectively Planck's constant and the speed of light, d the crystal lattice spacing and n an integer which specifies the diffraction order.

We already presented a prototype source based on Bragg diffraction, which exploits lead-glass capillary plates to constrain to 45° the incident and diffraction angles and small (2 W) X-ray tubes to produce the radiation to be diffracted (Muleri et al., 2007). This source was used to generate polarized photons at 2.6 keV, 3.7 keV and 5.2 keV and calibrate at these energies the GPD filled with a He-DME mixture (Muleri et al., 2008). An aluminum crystal and an X-ray tube with anode made of calcium were exploited to produce 3.7 keV polarized photons, while 2.6 keV and 5.2 keV were obtained by first and second order diffraction on graphite of copper X-ray tube radiation. The former configuration
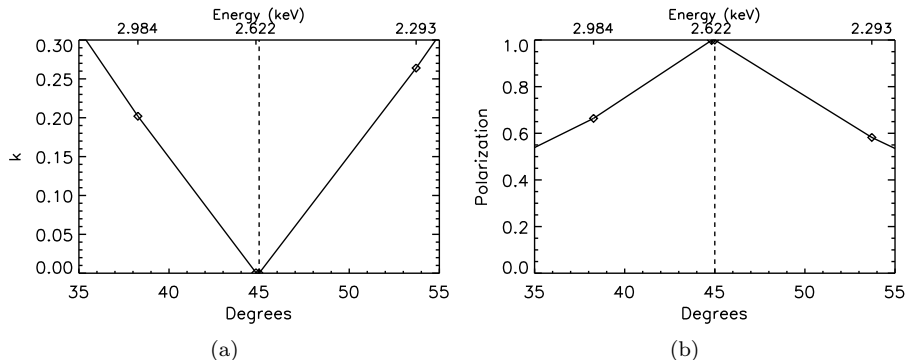
4

Figure 1: (**a**) Dependence of k with incident angle and energy, related by Bragg's law, for graphite crystals. The value of k was calculated by Henke et al. (1993) (**b**) Expected degree of polarization, derived from Equation (1).

is particularly effective in terms of higher flux and control of the output state of polarization because Kα fluorescence emission of calcium is well in accordance with Bragg energy at $45°$ for aluminum. Then (almost) all incident photons have a well-defined energy, that of Kα line of calcium, and are diffracted exactly at the Bragg angle given by Equation (2) and the degree of polarization is precisely calculated with Equation (1). A trade-off between flux (low collimation) and high polarization (high collimation) was instead necessary for diffraction on graphite because X-ray tubes with anodes in accordance with Bragg energy are not available in this case and continuum bremsstrahlung emission is to be used.

After the construction of this first prototype, we built a more powerful source based on the same concept but with some differences. The most important is that the crystal is mounted on a manual stage which allows two axes tilt regulation in the range $\pm 3°$ to achieve the best alignment to the Bragg condition. More crystals are available to produce radiation at different energies and, thanks to more powerful X-ray sources (50 W), a tight collimation can be retained even for diffraction of continuum radiation, which is less effective than the use of line in accordance to Bragg condition. A mechanical assembly combined with motorized and manual stages, which complete what we call X-ray facility, allows the detector to be moved, rotated and inclined with respect to the beam (see Figure 2).

Within the work presented in this paper, we used three different crystals, PET, graphite (grade D, $1.2°$ of mosaic spread) and aluminum. In the first two cases, we used the improved version of the Bragg source and exploited the diffraction of continuum photons produced by an X-ray tube with anode made of titanium, which has the thinnest window among our medium power tubes. We constrained both incident and diffraction angles on the crystal with two capillary plates which provide a collimation 1/40 (semiaperture $1.4°$) and 1/100 ($0.6°$) respectively. The PET crystal was used to generate 2.0 keV and 4.0 keV
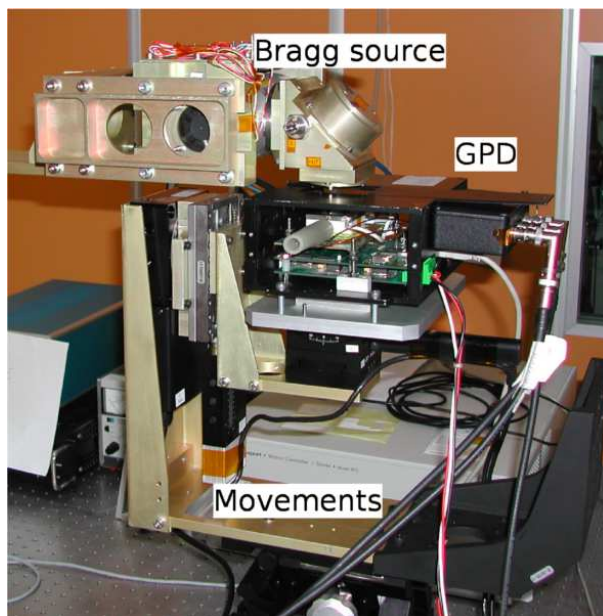
Figure 2: Setup of the measurements. X-rays, generated by a 50 W tube manufactured by Oxford Instruments, are emitted horizontally and diffracted downwards by a crystal oriented at $45°$. Two collimators constrain the divergence of the incident and of the diffracted photons and a diaphragm, placed after the second collimator, limits the size of the beam. The detector is mounted on a platform which is allowed to rotate, move and incline with respect to the incident beam with high precision, $< 1~\mu m$ for movements and < 1 arcsec for rotation/inclination.

Energy (keV)	Crystal	X-ray tube	Collimation	Diaphragm mm	$\mathcal{P}$
2.0 4.0	PET, 1st order PET, 2nd oder	Ti, 50 W	In: $\frac{1}{40}$, Out: $\frac{1}{100}$	$\varnothing$ 2	>0.99
2.6 5.2 7.8	GrD, 1st order GrD, 2st order GrD, 3st order	Ti, 50 W	In: $\frac{1}{40}$, Out: $\frac{1}{100}$	$\varnothing$ 2	>0.99
3.7	Al, 1st order	Ca, 2 W	Out: $\frac{1}{40}$	$\varnothing$ 2	0.9938

Table 2: Setup for each crystal. "GrD" stands for the mosaic graphite grade D crystal.

polarized radiation, corresponding to the first and second order of diffraction ($2d = 8.742$ Å, Henke et al., 1993), while for graphite we exploited the first three orders at 2.6 keV, 5.2 keV and 7.8 keV ($2d = 6.708$ Å, Henke et al., 1993). At 3.7 keV we used the prototype source because of the favorable accordance between the aluminum crystal and the Kα line of the calcium tube. In this case the geometry was already constrained by the use of nearly monochromatic incident photons and hence only a single collimator (with collimation 1/40) limited the diffraction angle. Helium flowing in the Bragg diffractometer was required with PET crystal to avoid severe air absorption of 2.0 keV photons. A diaphragm 2 mm in diameter was used to illuminate only the small central region of the detector. The setup for each crystal is summarized in Table 2.

Spectra diffracted by crystals were acquired by means of a Si-PIN Amptek XR100CR spectrometer with a energy resolution $\sim$200 eV FWHM at 5.9 keV. Lines were fitted with a gaussian profile and the measured line energy was used to estimate the degree of polarization $\mathcal{P}$ by the calculation of the diffraction angle and of the interpolated value of k. Thanks to the tight collimation of the two capillary plates on the incident and diffraction directions, the degree of polarization is always above 99%. The lack of any significant dilution of polarization is also confirmed by the narrowness of diffracted lines, which have a FWHM ($\sim$200 eV, 215 eV at 7.8 keV) consistent with that of fluorescence lines at comparable energies.

As an example, we report in Figure 3 the spectrum for diffraction on the graphite crystal of radiation generated by the titanium X-ray tube. The first three orders are prominent at 2.6 keV, 5.2 keV and 7.8 keV but from residuals is also evident a line at about 3.5 keV, which is the escape peak from silicon of the 5.2 keV photons, and a contribution at 4.5 keV. The latter is caused by Kα titanium fluorescence photons scattered on the crystal or on its holder and reaching the detector after passing through the two collimators. By the way, the two collimators are completely opaque at this energy and then only scatterings at nearly 90° are possible. This implies that even scattered photons are highly polarized perpendicularly to the scattering plane. Even if the GPD is not able to resolve this line and that at 5.2 keV, the flux of the former is $< 1/300$ than
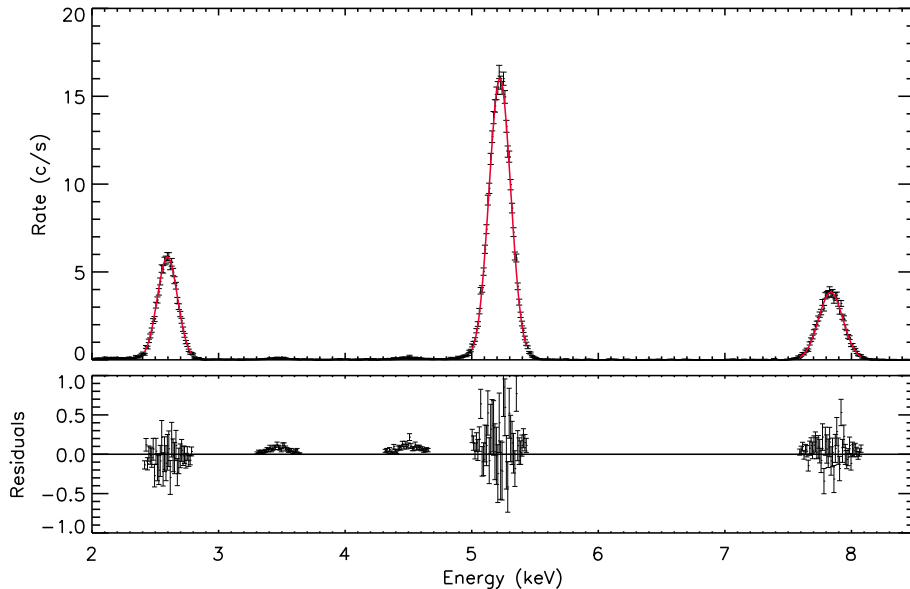
Figure 3: Spectrum obtained by diffraction on the graphite crystal of continuum photons produced with the titanium X-ray tube and acquired with the Amptek XR100CR spectrometer. The first three orders are visible at 2.6 keV, 5.2 keV and 7.8 keV and gaussian fits of each line are also reported as red solid lines. The high voltage of the X-ray tube was set to 10 kV to avoid the presence of photons at energies above the third order. The line at about 3.5 keV is the escape peak of 5.2 keV photons and that at 4.5 keV is the scattered titanium Kα.

that at 5.2 keV and therefore it will be neglected in the following.

3. Spectral capabilities

In Figure 4 we report the spectrum acquired with the GPD for monochromatic (and polarized) radiation obtained by Bragg diffraction on PET (2.0 keV and 4.0 keV) and graphite crystals (2.6 keV, 5.2 keV and 7.8 keV). Energy of photons is derived by the sum of the charge content of hit pixels. The lines are well resolved and this allows us to present in the next Section the modulation factor for each energy without any significant crosstalk. Lines are fitted with a Gaussian profile and the results are reported in Table 3. Data is filtered (i) to select spatially the incident beam and (ii) remove the tracks with two or more clusters of hit pixels, that is we postpone those events ($\lesssim$5%) which are composed of non-contiguous groups of pixels to subsequent refined analyses.

The relation between the energy and the pulse height, reported in Figure 5, is fitted with a line $y = mx + q$, where $q = (-239.7 \pm 2.3)$ ADC and $m = (1055.8 \pm 0.8)$ ADC/keV. The deviations from linearity (5% at 7.8 keV) can be explained by the insufficient control of high voltage values and/or the inadequate monitor of the environment conditions. The HV power supply used (CAEN N470) has a accuracy ± 1 V and a long term stability ± 2 V, which imply variations on the

8
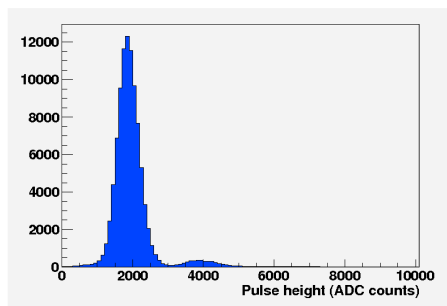
(a)
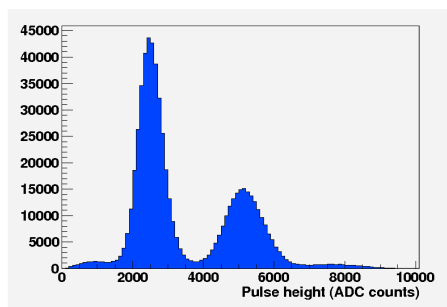
(b)

Figure 4: GPD spectrum of monochromatic photons at 2.0 keV and 4.0 keV (**a**) and at 2.6 keV, 5.2 keV and 7.8 keV (**b**).

Energy	E_{peak}	FWHM	$\delta E/E$
(keV)	(ADC)	(ADC)	(ADC)
2.0	1867 ± 1	689 ± 3	0.369 ± 0.002
2.6	2480 ± 1	797 ± 3	0.321 ± 0.001
3.7	3783 ± 2	1071 ± 4	0.283 ± 0.001
4.0	4013 ± 3	1104 ± 8	0.275 ± 0.002
5.2	5099 ± 3	1248 ± 8	0.245 ± 0.002
7.8	7645 ± 15	1793 ± 23	0.235 ± 0.003

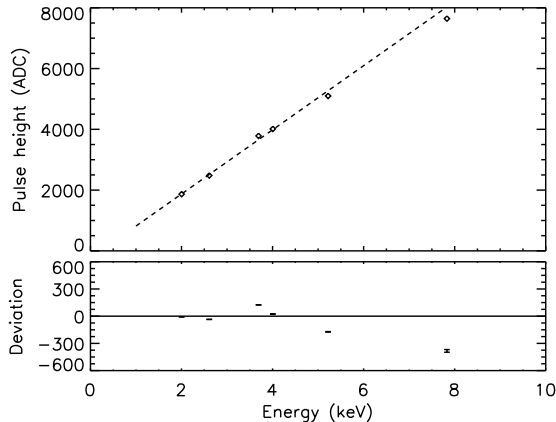Table 3: Results of the fit to the lines at different energies acquired with the GPD.

9

Figure 5: Energy calibration of the GPD.

gain of the order of $\pm 4\%$. The gain G can be normalized by temperature T and pressure p, expressed in Kelvin and torr respectively, with the function:

$$\frac{G^{corr}}{G^{meas}} = \frac{1}{\exp\left[C \times \left(\frac{1}{p/T} - \frac{1}{2.533}\right)\right]}, \tag{3}$$

where G^{meas} and G^{corr} are the measured and corrected values and C is a constant, equal to 19.1 Torr/K for the RIKEN-80T-LCP GEM (Tamagawa et al., 2009). Changes of temperature cause linear variations on the gain, $\Delta g \propto -\Delta T$, and fluctuations of 2 K, which are plausible in our case, results in gain instabilities of 5%.

Within Poisson or Poisson-like statistics of ionization and charge amplification (Knoll, 2000), the dependence of the energy resolution $\delta E/E = \text{FWHM}/E_{peak}$ as a function of energy is expected to be $\delta E/E \propto 1/\sqrt{E}$ for a gas detector. The relation in the case of the GPD is reported in Figure 6: although the energy resolution decreases with energy, the sole dependence with $1/\sqrt{E}$ is unsatisfactory. Therefore we used a function:

$$\frac{\delta E}{E} = \sqrt{\left(\frac{k_1}{\sqrt{E}}\right)^2 + (k_2\, E)^2}, \tag{4}$$

where $k_1 = (0.520 \pm 0.001)\,\sqrt{\text{keV}}$ and $k_2 = (0.0188 \pm 0.0005)\,\text{keV}^{-1}$ (dashed line in Figure 6). The fit function comprises two contributions summed quadratically, the first being the statistical Poisson noise in the ionization and amplification of the charges. We used the second term to model in a simple way an additional contribution which seems to weigh more at higher energy. A significant role within it could be played by incomplete charge collection due to photoelectron hits on the gas cell surfaces, which depends on the direction of emission but also on energy through the range (1 mm at 7.8 keV). We positioned the beam in the center of the detector, but loss of charge can still
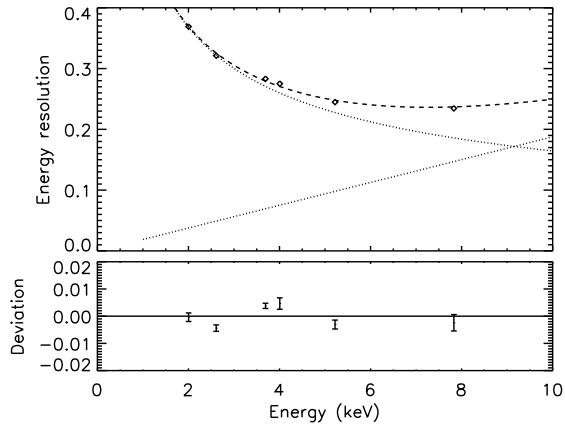
10

Figure 6: Energy resolution as a function of energy. The fit function (dashed line) takes into account the statistical noise and a linear contribution. These two terms are plotted with dotted lines.

occur if photons are absorbed near the window or the GEM. More energetic and hence longer tracks are also spread on larger regions of the GEM and of the ASIC and then nonuniformities could give a contribution. While the former have been reported at the level of several percent on spatial scales of a few millimeters (Tamagawa et al., 2009), we are confident that ASIC contribution is small if not negligible. Pedestals are read-out and substracted immediately after the event (delay of a few μs) and pixel noise is very low, 50 electrons ENC (Bellazzini et al., 2006). Tracks produced by photons at 2.0 keV hit on average 40 pixels (see below) and then the total contribution of electronic noise is of the order of $\sqrt{2}\ \sqrt{40}\ 50 \approx 450$ electrons, where the factor $\sqrt{2}$ is for pedestals substraction. Conversely, 2.0 keV photons produce 71 primary electrons, assuming that the average energy loss for the creation of a ion-electron pair in DME is 28 eV (Pansky et al., 1997), and Poisson fluctuations are $\sqrt{f\ 71}$, where f is the Fano factor $\sim$0.3 for DME (Pansky et al., 1997). After the GEM amplification of a factor 500 (see Table 1), statistical fluctuations result in 4800 electrons (Knoll, 2000), i.e. a factor 10 larger than electronic noise. Actually, we expect that the main source of the possible electronic contribution to energy resolution is the spatial nonuniformities in pixels gain, which can't be calibrated because sufficient precise test capacitances does not allow to be build with the 0.18 mm VLSI technology.

Spectral performance achieved is overall quite good. The energy resolution at 5.9 keV is less than 24% and then very close to the requirement of 20% for space missions that foresee a GPD on-board, which, however, assume that energy is measured with a dedicated spectroscopic channel taking the signal from the upper electrode of the GEM.

Interestingly enough, the average number of hit pixels $\langle p \rangle$ is a very well defined function of energy (see Figure 7). The dependency can be modelled
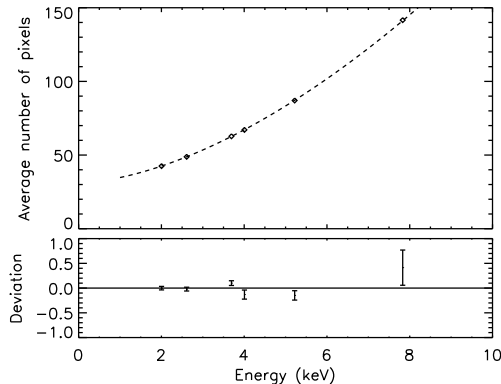
Figure 7: Average number of hit pixels per track p as a function of energy. Errors are evaluated as the ratio between the root mean square of the p distribution and the square root of counts.

with a function:

$$\langle p \rangle = k_a + k_b \ \left(\frac{E}{1 \text{ keV}} \right)^{k_c} , \tag{5}$$

with $k_a = (31.15 \pm 0.13)$, $k_b = (3.58 \pm 0.05)$ and $k_c = (1.664 \pm 0.008)$. Note that the index of the power law is broadly consistent with the energy dependence of electron range in a gas, reported to be $R = 0.71 \ E_{\text{MeV}}^{1.72} \ \text{g/cm}^2$ under a few hundred of keV by Sauli (1977).

In principle the Equation (5) could be exploited to derive an estimate of the photon energy, but unfortunately the correlation is rather weak because the number of hit pixels has also a strong dependence on the photoelectron direction of propagation. Photoelectrons emitted orthogonally to the collection plane produce smaller tracks than those which instead propagate mostly parallel. The errors associated to the energy determination by means of the Equation (5) could be derived precisely only by the knowledge of the probability function of p, but with an approximate gaussian fit the energy resolution is rather poor ($> 60\%$, about constant with energy).

4. Modulation factor

In general, the response of a polarimeter is modulated as a result of the absorption of polarized photons: the degree and the angle of polarization are derived from the amplitude and the phase of this modulation, respectively. The modulation curve $\mathcal{M}(\phi)$ of a photoelectric polarimeter is the number of photoelectrons emitted per each azimuthal angle ϕ. The direction of emission is most probably aligned with the electric field of the absorbed photon, the dependency being expressed by the differential cross section of the interaction (Heitler, 1954):

$$\frac{d\sigma_{ph}^K}{d\Omega} \propto \frac{\sin^2 \theta \cos^2 \phi}{(1 + \beta \cos \theta)^4}, \tag{6}$$

12

where β is the photoelectron velocity in units of c. θ and ϕ are the latitudinal and azimuthal emission angles, measured with respect to the direction of incidence and of polarization respectively. The formula reported above is valid only in the case of spherically symmetric shells, otherwise corrections which reduce the response to polarization are required (Ghosh, 1983). As far as the GPD is concerned, K-shell is largely the most probable involved in photoabsorption and then the Equation (6) is sufficiently accurate.

For completely polarized photons, the number of photoelectrons emitted in a certain direction is modulated as a $\cos^2$ function, while for partially polarized radiation the amplitude is reduced linearly. Real instruments do not respond perfectly to polarization, in the case of the GPD because of scatterings with nuclei, gas diffusion and finite size of ASIC pixels. Hence even for 100% polarized photons the amplitude of the response, called modulation factor μ, is never complete but it is calculated as:

$$\mu = \frac{\mathcal{M}_{max} - \mathcal{M}_{min}}{\mathcal{M}_{max} + \mathcal{M}_{min}}, \tag{7}$$

where $\mathcal{M}_{max}$ and $\mathcal{M}_{min}$ are the maximum and the minimum of the modulation, which practically is the histogram of photoelectron angles of emission, in the case of completely polarized photons. Since $\mathcal{M}(\phi)$ is fitted with a function $\mathcal{M}(\phi) = A + B \cos^2(\phi - \phi_0)$, then:

$$\mu = \frac{B}{2A + B}. \tag{8}$$

The modulation factor, and the efficiency ϵ, are the primary parameters used to derive the sensitivity of a polarimeter. The modulation measured, proportional to μ, is to be compared with that naturally arising from statistical Poisson fluctuations of the number of photoelectrons emitted per angular bin, which are inversely proportional to $\sqrt{\epsilon}$ if the background is negligible as for an experiment at the focus of an X-ray telescope. The product $\mu\sqrt{\epsilon}$ is called quality factor (see Muleri et al. (2008) for a more extended discussion on the sensitivity of a polarimeter). Within astrophysical application, the value of μ is especially important at low energy, where the largest part of photons are concentrated. Typical source spectra rapidly decrease with energy, as the efficiency of the instrument and the area of grazing incidence optics. For a Crab like spectrum between 2 keV and 10 keV and a standard (not multilayer) telescope, the $\sim$70% of counts are in the 2-3 keV energy range. For this reason, in the following we focus our attention on the performance at low energy.

4.1. Data analysis

The image of the photoelectron track is processed with an algorithm which reconstructs the absorption point as the center of gravity of the charge distribution (barycenter) and the direction of emission as that which maximizes the second moment (Bellazzini et al., 2003). The latter is basically the direction of elongation of the track. However, for energies higher than $\sim$3 keV, the initial
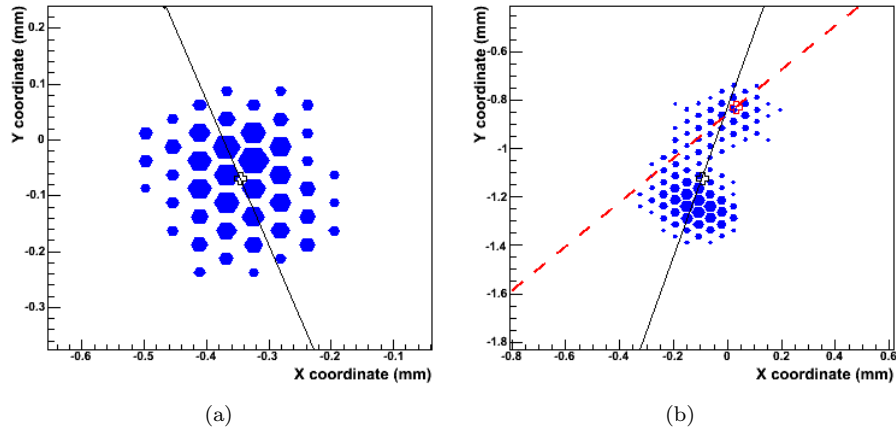
Figure 8: Examples of tracks at 2.0 keV (**a**) and 5.2 keV (**b**). The reconstructed direction of emission obtained by analyzing the entire track and resolving the first part are the black solid line and the red dashed one, respectively. The barycenter and the impact point are the black and the red crosses.

part of the track with lower ionization density (energy losses are inversely proportional to the energy) and the point where photoelectron is stopped (Bragg peak) are resolved. The algorithm selects the pixels at the edge of the track with the lower signal density and calculates the impact point and the maximum second moment, i.e. the direction of emission of the photoelectron, considering only these pixels. The initial direction of photoelectrons is used to create the histogram of emission angles, that is the modulation curve, which shows a $\cos^2$ modulation if the absorbed photons are polarized while it is flat for unpolarized radiation. Depending on the polarization degree to be detected, the modulation curve must be constructed with a large number of photons, at least several tens of thousands, to achieve a result which is statistically significant.

In Figure 8 we report two examples of tracks at 2.0 keV and 5.2 keV to show the effectiveness of our reconstruction algorithm. At low energy the track is so short that any substructure is blurred by diffusion during the drift in the gas cell. However a fraction of the original polarimetric information is still present in the elongation of the charge distribution, which is correlated with the initial direction of photoelectron emission as demonstrated by the measurement of a modulation factor value different from zero (see below). Instead, when tracks are more energetic and hence longer, the final part is clearly distinguished by the denser charge density. The direction reconstructed at the second step, reported as the red dashed line in Figure 8(b), is evidently a better approximation of the actual direction of emission than that obtained at the first step as the elongation of the charge distribution (black solid line in Figure). As a matter of fact, the improvement of the modulation factor, that is the response to polarization, achieved passing from the first to second step is 28% at 5.2 keV and 50% at 7.8 keV.
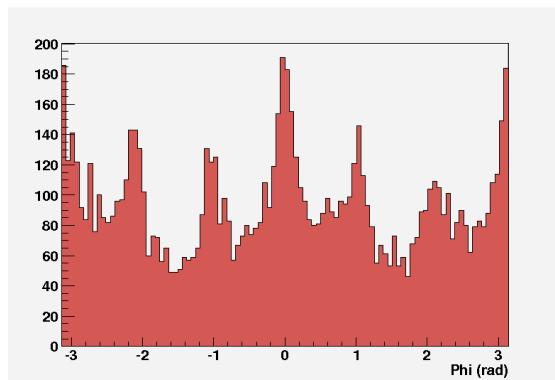
14

Figure 9: Systematic effects which emerge by selecting only tracks which hit less than 27 pixels at 2.0 keV. The 60° periodicity reflects the hexagonal pattern of the GEM, whose pitch is larger than usual.

Beyond selecting spatially the incident beam and excluding the tracks with more than one cluster, as explained in Section 3, we remove from the analysis on modulation factor those events which (i) hit less than 27 pixels and (ii) have an asymmetry less than a threshold that is different for each energy. The first cut is directly related to the GEM used, which has a pitch larger than usual (80 μm). When primary electrons are amplified by the GEM, the charges are constrained in the holes and this actually samples the event on the microscopic structure of the GEM. If the track is so short to involve only a few holes, the amplified charge distribution reflects significantly the GEM pattern. This is hexagonal and then produces on the elongation of the track, ultimately related to the reconstructed direction of emission, a systematic effect with periodicity 60°, namely the amplification makes most probable the directions aligned with GEM holes, which correspond to integer multiples of 60°. Pixels on the ASIC are arranged more finely than holes in the GEM (pitch 50 μm vs 80 μm) and removing those events which hit less than 27 pixels implies that we exclude from analysis tracks passed through only 10 GEM holes or less.

The modulation curve for events which hit less than 27 pixels is reported in Figure 9. The sharp peaks clearly mirror the hexagonal pattern of the GEM and significantly affect the total modulation curve because the fraction of events with less than 27 pixels is 10% at 2.0 keV (7.6% at 2.6 keV).

The asymmetry of a track (or eccentricity e) is defined as the ratio between the maximum and minimum values of the second moment of the charge distributions M^{II}, $e = M^{II}_{max}/M_{min}{}^{II}$. A higher value of e means that the track is more developed in a certain direction and then the information on the initial direction of emission is more preserved. On the contrary, almost round tracks ($e \approx 1$) have no preferred directions and then the large part of polarimetric information is lost.

We used the second cut on eccentricity to make our results comparable to what previously presented for the GPD filled with helium and DME by
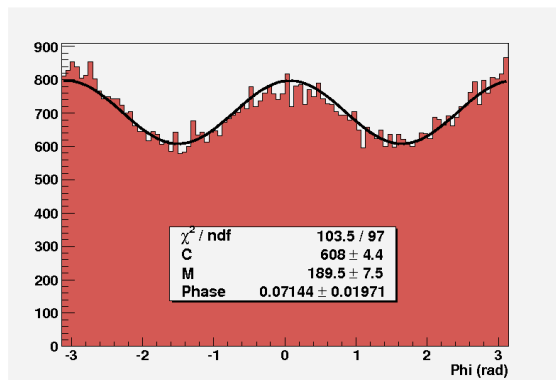
15

Figure 10: Modulation measured for 2.0 keV polarized photons.

Energy (keV)	μ	Cuts	FDR (%)	χ^2_ν	Counts
2.0	0.135 ± 0.005	$\#_p > 27, e > 1.18$	23.5	1.1	70379
2.6	0.267 ± 0.004	$\#_p > 27, e > 1.20$	22.0	1.6	91055
3.7	0.402 ± 0.003	$\#_p > 27, e > 1.39$	24.4	1.3	88968
4.0	0.426 ± 0.006	$\#_p > 27, e > 1.48$	24.4	1.2	27279
5.2	0.496 ± 0.005	$\#_p > 27, e > 2.00$	23.8	0.8	46141
7.8	0.589 ± 0.010	$\#_p > 27, e > 3.70$	24.4	0.9	9112

Table 4: Modulation factor measured at different energies. Cuts are applied on the number of hit pixels ($\#_p$) and on the eccentricity of tracks e. The fraction of data removed (FDR), the reduced χ^2_ν of the $\cos^2$ fit (97 d.o.f.) and the counts after cuts are also reported.

Muleri et al. (2008). These authors reported the modulation factor with different data selections aimed to optimize the quality factor $\mu\sqrt{\epsilon}$, and, from that analysis, best results were obtained by removing about 25% of events. In this paper we follow a specular approach as for previous measurements, we change the cut on the asymmetry of tracks to exclude from analysis about 25% of tracks to maximize the quality factor.

4.2. Comparison to Monte Carlo results and other mixtures

An example of the modulation curve obtained at 2.0 keV, particularly significative because it refers to the lowest energy at which a photoelectric polarimeter has ever been tested, is reported in Figure 10. At this energy the modulation factor is 13.5%, while the values measured at other energies are reported in Table 4.

Measured modulation factor is compared to the estimates derived from Monte Carlo simulations in Figure 11. Noteworthily we achieved expected performance at low energy (even if with modest cuts), while at higher energies measured values are systematically lower than expected. This discrepancy is quite small, $\lesssim 10\%$, and actually does not impact on the sensitivity of the in-
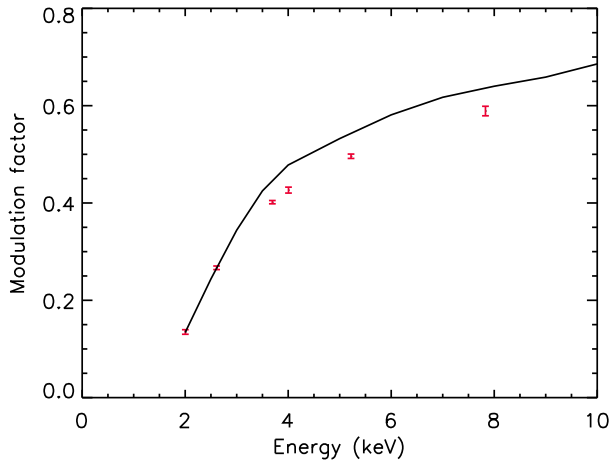
Figure 11: Measured values of the modulation factor (red points) compared with Monte Carlo results (solid line).

strument because emission from astrophysical sources is strongly concentrated at low energy where expected performance is entirely confirmed. Nonetheless this issue is probably a signature that Monte Carlo can still be refined and the discrepancy will be investigated to exploit in the best way the whole energy range of the instrument. The measurement of possible variations of polarization signature with energy is at the basis of the success of a X-ray polarimetry mission and the exploitation of the largest energy range possible, even better if it extends the "classical" 2-10 keV energy interval, is mandatory.

Finally it is useful to compare the modulation factor of the GPD presented in this paper with that already reported by Muleri et al. (2008) for a mixture composed of 20% helium and 80% DME at 1 atm. Despite the fact that the partial pressure of DME is (almost) the same for the two gases, there are some differences. While at lower energies the behavior is quite similar, the DME mixture apparently is less effective at high energy and at 5.2 keV the quality factor is $\sim$10% lower. Hence the presence of a small fraction of helium seems to favor reconstruction of longer tracks.

5. Conclusion

The characterization of the GPD presented in this paper represents one step forward to the optimization of the instrument as a photoelectric polarimeter. In place of the standard mixture composed of a small fraction of helium (20%) and DME (80%) at 1 atm, we tested the GPD filled with pure DME at 0.79 atm. Measured modulation factor successfully confirms Monte Carlo simulations at lower energy, while above 3.7 keV there is a discrepancy $\lesssim$10% with respect both the expected value and the sensitivity measured for the (similar) standard mixture. Although this issue does not significantly affect the performance of

17

DME, this work			He-DME	
Energy (keV)	μ	$\mu\sqrt{\epsilon}$	μ	$\mu\sqrt{\epsilon}$
2.0	0.135 ± 0.005	0.058 ± 0.002	—	—
2.6	0.267 ± 0.004	0.103 ± 0.001	0.276 ± 0.014	0.101 ± 0.005
3.7	0.402 ± 0.003	0.105 ± 0.001	0.431 ± 0.012	0.107 ± 0.003
4.0	0.426 ± 0.006	0.101 ± 0.001	—	—
5.2	0.496 ± 0.005	0.082 ± 0.001	0.545 ± 0.010	0.091 ± 0.002
7.8	0.589 ± 0.010	0.053 ± 0.001	—	—

Table 5: Comparison of the modulation factor μ and quality factor $\mu\sqrt{\epsilon}$ measured for DME at 0.79 atm and a mixture He 20% and DME 80% at 1 atm presented by Muleri et al. (2008).

the GPD, which are mostly determined at low energy, it deserves further investigations to exploit in the best way the whole energy range of the instrument. Conversely the modulation factor measured at 2.0 keV, the lowest energy ever presented for a photoelectric polarimeter, is relatively large, 13.5%, and encourages attempts to reduce the threshold of the instrument below this energy value. This could allow to address interesting scientific objectives, like the study of the (possibly) highly polarized thermal emission from the surface of cooling neutron stars.

We also discussed, for the first time in a systematic way, the spectral capabilities of the GPD. The spectrum of absorbed photons is obtained by summing the charge content of hit pixels and, in principle, it could be heavily affected by nonuniformities in the response of the pixels. As a matter of fact, the energy resolution is quite good, 24% at 5.9 keV, that is very close to that of standard proportional counters and to the requirement (20%) defined for future space missions that include the GPD. The dependency with energy, beyond a $1/\sqrt{E}$ contribution that is naturally explained as due to Poisson fluctuations in production and amplification of primary charges, shows an additional term whose origin will be subject of further investigation.

In conclusion, DME appears as an interesting alternative to mixtures of helium and DME. Despite the small reduction of the modulation factor at high energy, performance at low energy is confirmed. Possibly even more important, DME provides very good spectral capabilities, which are a mandatory complement of the polarimetric sensitivity to pursue the scientific objectives of any X-ray polarimetry mission.

Acknowledgments

Bellazzini, R., Angelini, F., Baldini, L., Brez, A., Costa, E., Di Persio, G., Latronico, L., Massai, M. M., Omodei, N., Pacciani, L., Soffitta, P., Spandre, G., 2003. Novel gaseus X-ray polarimeter: data analysis and simulation. In: Proc. of SPIE. Vol. 4843. p. 383.

Bellazzini, R., Brez, A., Minuti, M., Pinchera, M., Spandre, G., Muleri, F., Costa, E., Di Cosimo, S., Fabiani, S., Lazzarotto, F., Rubini, A., Soffitta, P., 2010 in press. A polarimeter for IXO. In: X-ray Polarimetry: A New Window in Astrophysics.

Bellazzini, R., Spandre, G., Minuti, M., Baldini, L., Brez, A., Cavalca, F., Latronico, L., Omodei, N., Massai, M. M., Sgro', C., Costa, E., Soffitta, P., Krummenacher, F., de Oliveira, R., 2006. Direct reading of charge multipliers with a self-triggering CMOS analog chip with 105 k pixels at 50 μm pitch. Nuclear Instruments and Methods in Physics Research A 566, 552.

Bellazzini, R., Spandre, G., Minuti, M., Baldini, L., Brez, A., Latronico, L., Omodei, N., Razzano, M., Massai, M. M., Pesce-Rollins, M., Sgró, C., Costa, E., Soffitta, P., Sipila, H., Lempinen, E., 2007. A sealed Gas Pixel Detector for X-ray astronomy. Nuclear Instruments and Methods in Physics Research A 579, 853.

Black, J. K., Baker, R. G., Deines-Jones, P., Hill, J. E., Jahoda, K., 2007. X-ray polarimetry with a micropattern TPC. Nuclear Instruments and Methods in Physics Research A 581, 755.

Costa, E., Bellazzini, R., Tagliaferri, G., Matt, G., 2010 in press. Programs of X-ray polarimetry in Italy. In: X-ray Polarimetry: A New Window in Astrophysics.

Costa, E., Soffitta, P., Bellazzini, R., Brez, A., Lumb, N., Spandre, G., 2001. An efficient photoelectric X-ray polarimeter for the study of black holes and neutron stars. Nature411, 662.

Evans, K. D., Hall, R., Lewis, M., 1977. The calibration of Bragg X-ray analyser crystals for use as polarimeters in X-ray astronomy. Space Science Instrumentation 3, 163.

Ghosh, P. K., 1983. Introduction to Photoelectron Spectroscopy. John Wiley & Sons.

Heitler, W., 1954. Quantum theory of radiation. International Series of Monographs on Physics, Oxford: Clarendon, 1954, 3rd ed.

Henke, B. L., Gullikson, E. M., Davis, J. C., 1993. X-Ray Interactions: Photoabsorption, Scattering, Transmission, and Reflection at E = 50-30,000 eV, Z = 1-92. Atomic Data and Nuclear Data Tables 54, 181.

Knoll, G. F., 2000. Radiation Detection and Measurement. Wiley; 3 edition (January 5, 2000).

Muleri, F., Soffitta, P., Baldini, L., Bellazzini, R., Bregeon, J., Brez, A., Costa, E., Frutti, M., Latronico, L., Minuti, M., Negri, M. B., Omodei, N., Pesce-Rollins, M., Pinchera, M., Razzano, M., Rubini, A., Sgró, C., Spandre, G., 2008. Low energy polarization sensitivity of the Gas Pixel Detector. Nuclear Instruments and Methods in Physics Research A 584, 149.

Muleri, F., Soffitta, P., Bellazzini, R., Brez, A., Costa, E., Fabiani, S., Frutti, M., Minuti, M., Negri, M. B., Pascale, P., Rubini, A., Sindoni, G., Spandre, G., 2007. A very compact polarizer for an X-ray polarimeter calibration. In: Proc. of SPIE. Vol. 6686. p. 668610.

Pansky, A., Breskin, A., Chechik, R., 1997. Fano factor and the mean energy per ion pair in counting gases, at low x-ray energies. Journal of Applied Physics 82, 871.

Sauli, F., 1977. Principles of Operation of Multiwire Proportional and Drift Chambers. Lectures given in Academic Training Program of CERN, 1975-1976 77-09.

Sauli, F., 1997. GEM: A new concept for electron amplification in gas detectors. Nuclear Instruments and Methods in Physics Research A 386, 531.

Tamagawa, T., Hayato, A., Asami, F., Abe, K., Iwamoto, S., Nakamura, S., Harayama, A., Iwahashi, T., Konami, S., Hamagaki, H., Yamaguchi, Y. L., Tawara, H., Makishima, K., 2009. Development of thick-foil and fine-pitch GEMs with a laser etching technique. Nuclear Instruments and Methods in Physics Research A 608, 390.